Bio-Design and Manufacturing (2020) 3:71–82
https://doi.org/10.1007/s42242-020-00063-x

RESEARCH ARTICLE

Computer-aided CT image processing and modeling method for tibia microstructure

Pengju Wang[1] · **Su Wang**[2]

Received: 2 December 2019 / Accepted: 24 January 2020 / Published online: 4 February 2020

Abstract

We present a method for computed tomography (CT) image processing and modeling for tibia microstructure, achieved by using computer graphics and fractal theory. Given the large-scale image data of tibia species with DICOM standard for clinical applications, we take advantage of algorithms such as image binarization, hot pixel removing and close operation to obtain visually clear image for tibia microstructure. All of these images are based on 20 CT scanning images with 30 μm slice thickness and 30 μm interval and continuous changes in pores. For each pore, we determine its profile by using an improved algorithm for edge detection. Then, to calculate its three-dimensional fractal dimension, we measure the circumference perimeter and area of the pores of bone microstructure using a line fitting method based on the least squares. Subsequently, we put forward an algorithm for the pore profiles through ellipse fitting. The results show that the pores have significant fractal characteristics because of the good linear correlation between the perimeter and the area parameters in log–log scale coordinates system, and the ratio of the elliptical short axis to the long axis through ellipse fitting tends to 0.6501. Based on support vector machine and structural risk minimization principle, we put forward a mapping database theory of structure parameters among the pores of CT images and fractal dimension, Poisson's ratios, porosity and equivalent aperture. On this basis, we put forward a new concept for 3D modeling called precision-measuring digital expressing to reconstruct tibia microstructure for human hard tissue.

Keywords Tibia · CT image processing · Fractal dimension · Support vector machine · 3D modeling

Introduction

In tibial tissue engineering, an ideal tibial tissue scaffold needs to be able to guide cells to form the bone tissues with mechanical, biological, and chemical functions. This tibial tissue scaffold provides the cellular environment for cell attachment, proliferation, and differentiation [1]. In addition, the behavior of cells is also affected by the molecular compositions of these contact positions and their spatial distributions [2]. Thus, creating porous scaffolds that mimic the complex structure of the natural tibia is one of the critical strategies in tibial tissue engineering [3]. Various methods have been used to successfully construct scaffolds with high porosity, including gas foaming [4], freeze-drying [5], and electrospinning [6]. However, these methods are difficult to precisely control the pore size, porosity, pore shape, and pore interconnectivity [7]. CT scanning is a continuous multilayer lossless image technology in micron scale. In recent years, along with the development of additive manufacture techniques, it has been successfully applied to qualitative and quantitative analysis and 3D modeling of medical images [8, 9]. Based on the method of threshold value division and region growth for CT image, the 3D models of tibia microstructure are reconstructed by using software Mimics. The main disadvantages of the CT-based modeling method are difficult reconstruction, a few hot pixels and impossible model in real time [10, 11]. Note that the usual reconstructed prosthesis does not match the anatomical features of patient's pathological parts.

In order to overcome the above challenges, it is feasible to construct the porous structure by the parameters derived from the microstructure of nature tibia tissues. We mainly focus on how to reconstruct individualized 3D models for

✉ Pengju Wang
wangpengju188@163.com

[1] School of Mechanical Engineering, Harbin Institute of Technology, Harbin, China

[2] School of Mechanical Engineering, Sichuan University, Chengdu, China

tibia microstructure with respect to its internal structure, permeability, porosity, and connectivity in this work.

Research works on the modeling of black box for CT image about support vector machine are too few. Mandelbrot [12] defined the fractal dimension as a set of wireless hierarchical and self-similarity structures. In this paper, we got CT images with high resolution through digital image processing, the methods of island and machine vision technology. For each image, we put forward an algorithm of image preprocessing, an improved algorithm for edge detection and an algorithm of ellipse fitting the pores, through spatial and frequency domain methods. All algorithms were based on the method of minimal threshold. By calculating its fractal dimension, we put forward a 3D identification modeling structure of the CT image with support vector machine. The research results are of great theoretical and practical value in clinical application for bone microstructures.

Overall parameter measurement method and design framework

Tibial microstructure incorporates elliptical cross section. The overall framework is proposed in this article. It instructs the parameter measurement and modeling of tibia with bioimitability and adaptability (Fig. 1). It consists of several steps in the following paragraphs and is further described in the next section. The so-generated cross sections of the microstructure are adapted to meet the individualized needs of different patients. By adopting this process, researchers can get individualized bone microstructure parameters. In this paper, more details are given by the measurement and modeling methods of structural parameters, such as image processing and ellipse fitting algorithm, and modeling based on support vector machine.

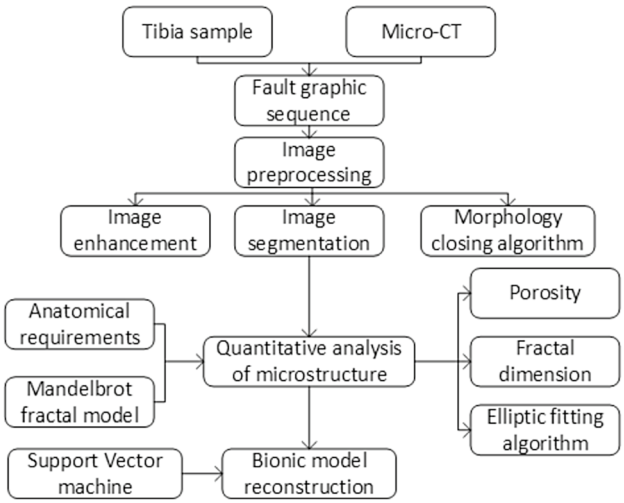

Fig. 1 Road map of computer-aided modeling

Design edge detection algorithm According to the fault graphic sequence from tibia sample, hot pixels of the images must be reduced to improve the definition and extract the edge of pore profiles. Thus, based on sample, quantization and the definition and resolution of CT images, we carried out image format conversion, image enhancement, gray and morphological transformation in sequence through spatial and frequency domain algorithms. On the bases, based on Sobel operator for edge detection, an improved algorithm is proposed to obtain clear outline shapes of edge of the holes.

Design elliptic curve-fitting algorithm According to the graphics after image processing, the accurate fitting structure must be obtained for parametric modeling. Therefore, we propose an elliptic curve-fitting algorithm to fit the pores, with the central point, long- and short-axis parameters being considered.

Modeling method To reconstruct bone microstructure, the proportion of ellipse corresponding to the area interval of adjacent regions is obtained by edge detection and elliptic curve-fitting algorithm. Based on the parameters of circumference and area of the pores, we get fractal dimension of the case of tibia microstructures. And we calculate the structural parameters, such as fractal dimension. Then, we propose a modeling method based on support vector machine. Subsequently, we show a modeling experiment as an example to support conclusion and confirm the reliability of the method.

Algorithm design

Preprocessing algorithm

For each image, its gray value is from 0 to 65,536. It is known that the DICOM format data from CT scanning contain information of patients, the level and width of current window. Based on the window level and width, we skipped the above information features and transformed DICOM into Bmp format by reducing the gray value to the range from 256 to 512. That is the general gray value of images displayed on screen through grayscale linear transformation. The linear gray transformation function is as follows:

$$D_{\mathrm{B}} = \begin{cases} D_{\max} & D_{\mathrm{A}} \geq C - 0.5 + \frac{W-1}{2} \\ \frac{(D_{\mathrm{A}} - C + 0.5)}{W-1}\left(D_{\max} - D_{\min}\right) & \text{the rest} \\ D_{\min} & D_{\mathrm{A}} \leq C - 0.5 - \frac{W-1}{2} \end{cases} \quad (1)$$

where D_{B} is the gray scale of BMP image; D_{A} is the gray scale of input image; C is the window level; W is the window width; $D_{\max}$ is the maximum gray value of display screen; and $D_{\min}$ is the minimum gray value of display screen.

We got the CT images in black and white. It is known that the discernability for the change in gray scale of pore is lower than color image [13]. Therefore, we converted the black and white images into color images to easily distinguish the edge of pore contours. Then, we selected the pore structures with gradient. Based on color transformation of gray scale in space domain, we mixed the RGB three-element color into different colors by using MATLAB. Figure 2a presents the original image before conversion. Figure 2b presents the color compensation effect when the gray value between 60 and 105 is set as blue compensation, between 105 and 150 is set as green compensation and greater than 150 is set as red compensation.

The two-dimensional gray scale of tibia microstructure is distinguished by the relative size of the gray value and the threshold value of pixel for CT images. The grayscale transformation is as follows:

$$g(x,y) = \begin{cases} 1 & f(x,y) \geq T \\ 0 & f(x,y) < T \end{cases} \tag{2}$$

where $g(x, y)$ is the output image; $f(x, y)$ is the input image; and T is the threshold.

To count the number of gray values corresponding to pixel, Fig. 3a presents the gray histogram consisting of 64 grayscale intervals. The results exhibit two obvious peaks, but the accurate value of the valley area is difficult to be obtained. In this experiment, the histogram is fitted in a curve, and the threshold is preliminarily determined based on minimum threshold method. The equation of minimum point is as follows:

$$\begin{cases} p'(z) = 0 \\ p''(z) > 0 \end{cases} \tag{3}$$

where $p'(z)$ is the first derivative of curvilinear equation and $p''(z)$ is the second derivative of curvilinear equation.

Figure 3b presents the normalized histogram of 32 grayscale intervals. The final segmentation threshold is determined to be 60 by counting and optimizing the ratio of the number of pixels falling into each interval to the total number of pixels.

We preliminarily eliminated the hot pixels of images by median filtering and smoothed the images by Gaussian low-pass filtering. K_1 is the 1442×1840 grayscale matrix image before median filtering. K_2 is the 1442×1840 grayscale matrix image after median filtering with 7×7 window.

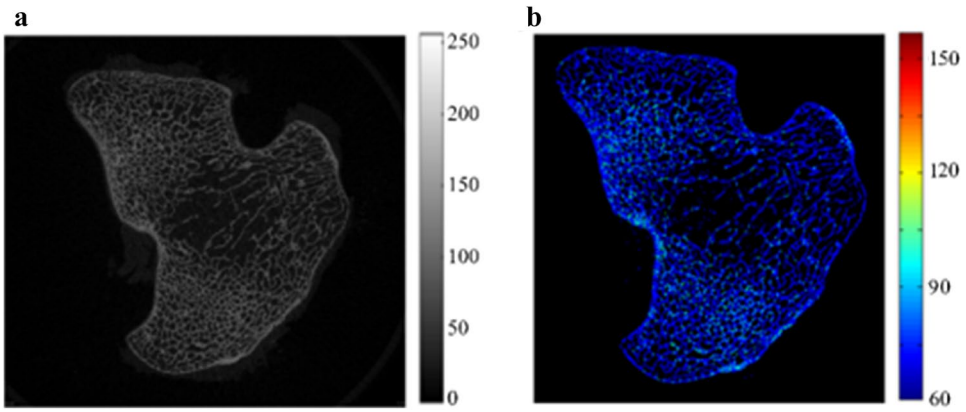

Fig. 2 Illustration of the effect of color enhancement for CT images. **a** The original image before conversion; **b** the effect of color image enhancement after conversion

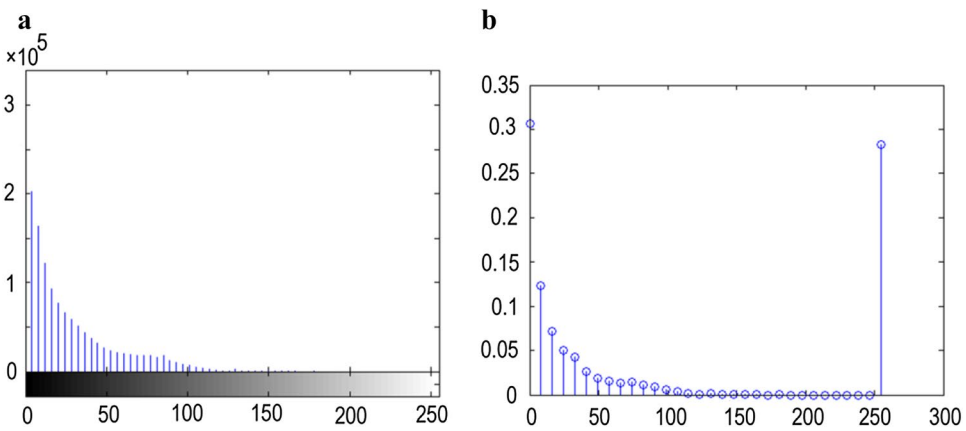

Fig. 3 Determining the segmentation threshold of CT images. **a** The gray histogram; **b** the normalized histogram

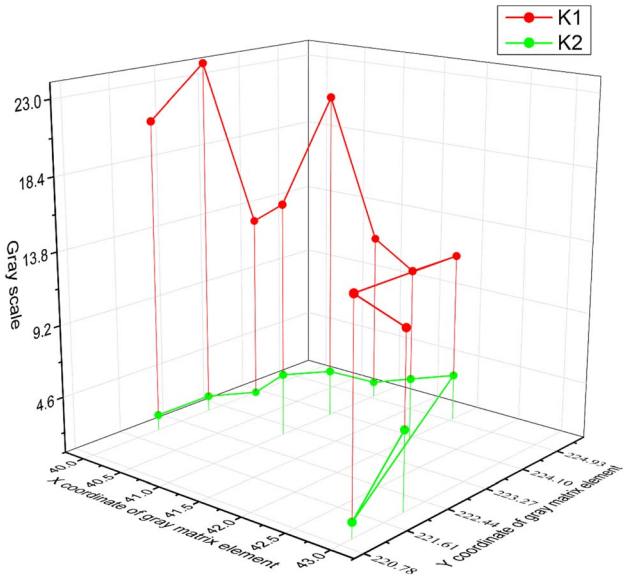

Fig. 4 Filtering effect before and after median filtering

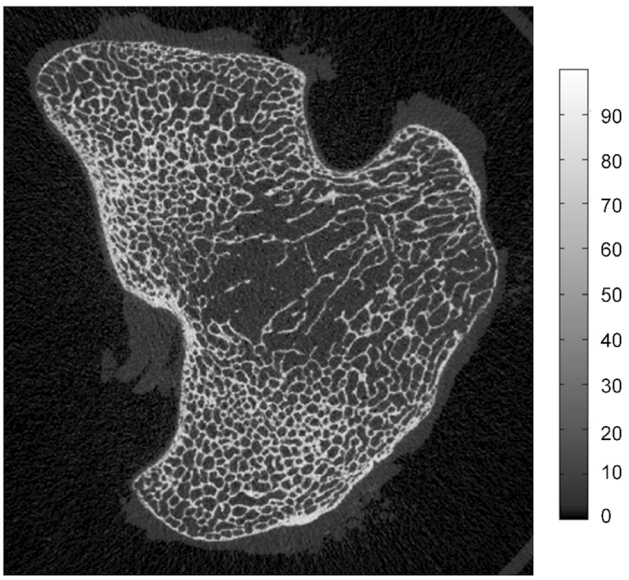

Fig. 5 Illustration of the effect of Gaussian high-pass filter while Sigma is set to 300

Figure 4 intuitively represents the filtering effects. The experimental results show that the noises are obviously reduced in K_2.

Figure 5 presents the filter effect of the image filtered by a Gaussian low-pass filtering with Sigma parameter set to 300. In order to further verify the filtering effect with the above methods, the spectrum diagram of the image is obtained by fast Fourier transform. Figure 6a presents the spectrum diagram of the original image distributed uniformly with many high-frequency sections. And Fig. 6b presents the spectrum diagram of Fig. 5 around the center with many low-frequency sections. The distribution of the spectrum of processing image after median and Gaussian high-pass filter is more uniform. So we could say some details in the image are eliminated by the filtering and the edge parts of pore profile of the original image are preserved.

Based on the above extracted images, the image pixels with threshold greater than T are set to 1 and others are set to 0. We set the boundary contours of pores of the image part to white and background part to black. Figure 7 presents the binary image after binary processing from original image. In Fig. 7, all structures are different such as the unclosed pore boundaries and incoherent edges. Closed operation is defined as expansion followed by corrosion. After the binarized image was processed by using the operation, we created a disk-shaped structural element with a radius of three, then filled the edge and closed the fracture to get the closed pore boundary contour.

An improved algorithm for edge detection

Bhargav et al. [14] introduced many operators for edge detection. In this section, we discuss some algorithms for edge detection for tibia microstructure. Figure 8 presents the edge-detected image after preprocessing by using Roberts operator, Prewitt operator, LOG operator, Canny operator, Sobel operator, respectively.

The experimental results are shown as follows: The image edges extracted by using Roberts operator lack the detailed contour; many details and low-contrast image edges are extracted by using LOG operator; oversmoothness images extracted by using Canny operator are oversmoothing and relatively weak for the detection of low-contrast edges; relying on larger templates, the Sobel and Prewitt operators are capable of smoothing, removing hot pixels, and false edges, while smoothing the useful edges as well. The images extracted after edge detection by using Sobel operator are clearer and more accurate than those extracted by using Prewitt operator, but some hot pixels remain.

Therefore, we proposed an improved algorithm based on Sobel operator for edge detection. We processed the binarized image by morphological closed operation based on the disk structural elements with a radius of 4. Then, we performed median filtering with a 3×3 matrix template. And finally, we extracted edges by using Sobel operator. Figure 8 presents the compared image with Sobel operator and its improved operator. By comparing the image processed by the improved Sobel operator with this processed by original Sobel operator, we can find that the image processed by the improved Sobel operator is better. A lot of noise points and false edges are removed, and the effect of background purification is particularly obvious. As shown in Fig. 8f, the outline shape of edges of the holes is clearer, with more

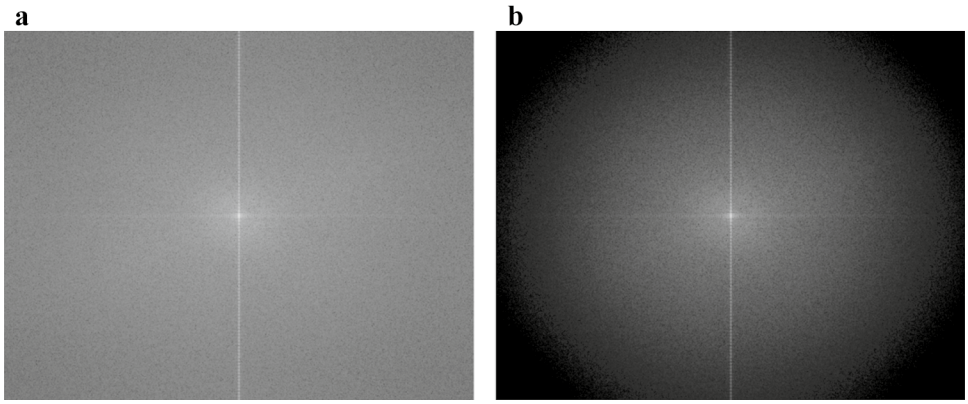

Fig. 6 Illustration of the effect of spatial and frequency domain filtering. **a** The spectrum of original image; **b** the spectrum of processing image after median and Gaussian high-pass filter

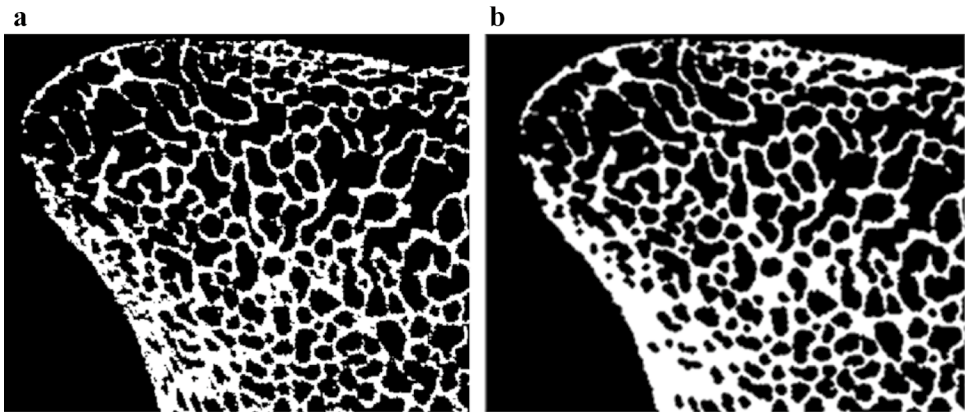

Fig. 7 Illustration of close operation defined as expansion followed by corrosion. **a** Before close operation; **b** after close operation

surface-to-surface contacts, less voids, and clearer mosaic contours and free holes. The pore structure is easy to be modeled by parameterizing, so it has good constructability. In addition, only contour information of the pores including hot pixels, false edges and minimal aperture is neglected and porosity still meets the design requirement. What's more, higher pore size improves bone ingrowth within a certain range [15]. So it has no significant impact on the reliability of modeling. The experimental results show that the improved Sobel algorithm is better than the original algorithm in detecting the pore edge profile of tibial microstructures. Based on the above planar structure, we reconstructed a three-dimensional bionic model that satisfies mechanical intensity.

We obtained 659 simply connected regions by filling the holes edge detection and deleting the elements connected to the boundary of the image. Then, we accurately measured the attribute parameters of area, centroid, long axis and short axis of ellipse and the angle between the major axis and the *X*-axis of each elliptical object under pixel units.

It is observed that the proportion in the area of apart elliptical objects is smaller than other ellipses after filling holes, and the area of each part is different. So, it is difficult to build its microstructural database. Higher porosity and pore size result in lower mechanical properties, but improve bone ingrowth [15]. The suitable porosity and pore size are the key elements for the normal physiological function of the constructed transplantable tibial substitute in the design of 3D bone tissue scaffolds. In this paper, the porosity of microstructure is ensured to meet the physiological requirements. We ignored the ellipses of area value less than the average area value of all the ellipses and obtained 184 simply connected regions. The distribution of each ellipse in the corresponding space was counted by using hierarchical classification method. Figure 9 presents the number of ellipses in the corresponding interval at 1400× magnification. It is observed that the number of ellipses decreases as the elliptical area increases, and the proportion of its total number is 68% in the range from 200 to 600. So the number of ellipses has large quantities.

An algorithm for ellipse curve fitting

The internal microstructures of the scaffold may have an important effect on the cellular microenvironment. Microenvironment, including three-dimensional structure of bone scaffold, biochemical compound and mechanical stimulation, plays a critical role in guiding osteocyte proliferation and differentiation [16, 17]. Thus, mimicking structures of the native bone may contribute to

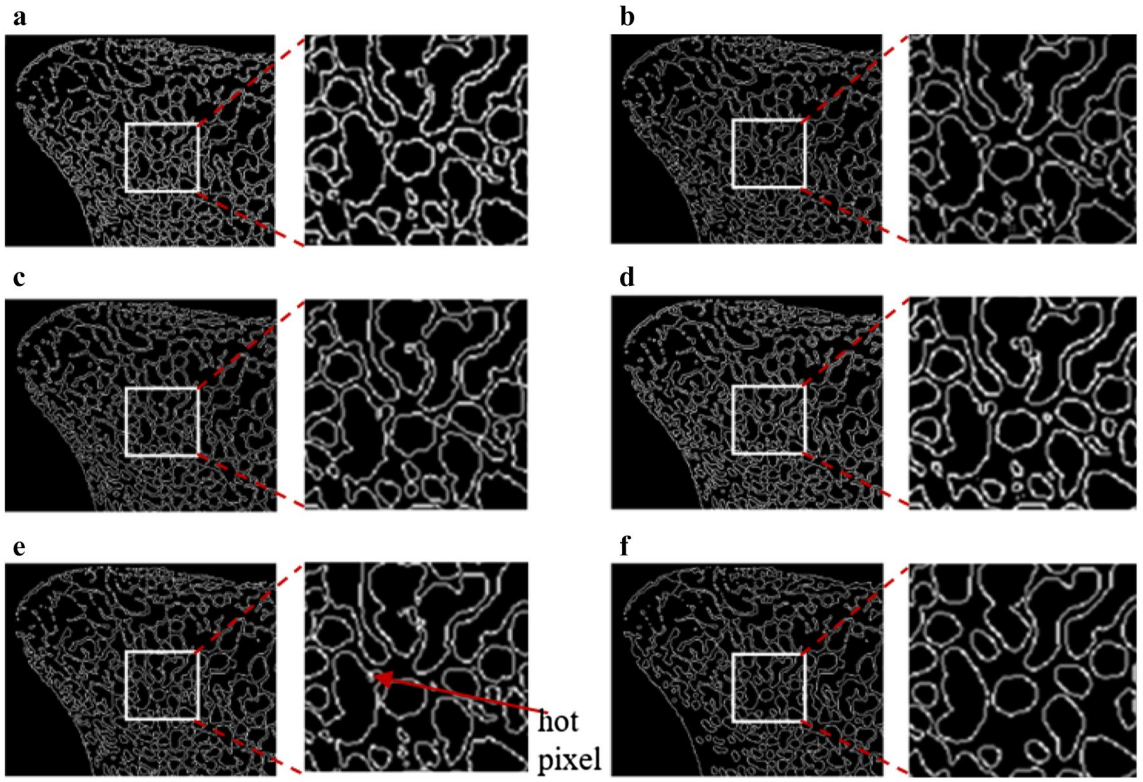

Fig. 8 Comparison of the effect of several algorithms. **a** Roberts operator; **b** Prewitt operator; **c** LOG operator; **d** Canny operator. **e** Sobel operator, and **f** an improved Sobel algorithm

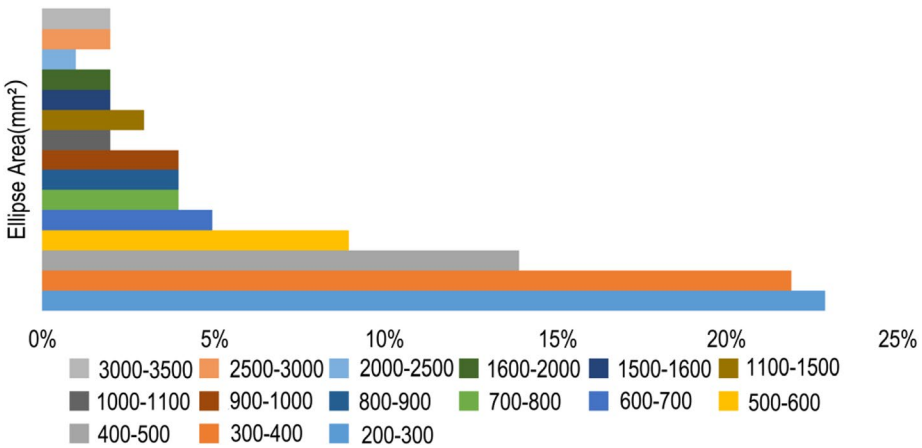

Fig. 9 Proportion statistics of the ellipse corresponding to area interval of simply connected regions at ×1400 magnification

constructing the porous scaffold with biocompatibility. In order to analyze the distribution characteristics of the native tibia, we got the image of proximal tibial intersecting surface by micro-CT scanning, image binarization, and removing noises above. Silva et al. [9] introduced that the point on the cross section of bone trabecular can be represented accurately by ellipse interpolation. We fit the pores through ellipse and take the center coordinates of the scatter obtained from circle fitting as the elliptical centroid coordinates. Based on the elliptic center satisfying the point equation of curve, the relation of the scatter satisfying elliptic standard equation is as follows:

$$\begin{cases} Ax^2 + By^2 - AB = 0 \\ x^2 + ax + y^2 + by + c = 0 \end{cases} \tag{4}$$

The elliptic equation above is transformed as follows:

$$ax_i + by_i + c = -\left(x^2 + y^2\right) \tag{5}$$

Based on the three unknowns and far more than three scatter points in the equation, we transformed the above equation into a matrix form of multiple scatter as follows:

$$CX_1 = D \tag{6}$$

$$\text{where } C = \begin{bmatrix} x_1 & y_1 & 1 \\ x_2 & y_2 & 1 \\ \cdots & \cdots & \cdots \\ x_n & y_n & 1 \end{bmatrix}; X_1 = \begin{bmatrix} a \\ b \\ c \end{bmatrix}; D = -\begin{bmatrix} x_1^2 & y_1^2 \\ x_2^2 & y_2^2 \\ \cdots & \cdots \\ x_n^2 & y_n^2 \end{bmatrix}.$$

In the same way, Eq. (5) is transformed as follows:

$$EX_2 = F \tag{7}$$

$$\text{where } E = \begin{bmatrix} x_1^2 & y_1^2 \\ x_2^2 & y_2^2 \\ \cdots & \cdots \\ x_n^2 & y_n^2 \end{bmatrix}.; X_2 = \begin{bmatrix} A \\ B \end{bmatrix}; F = \begin{bmatrix} AB \\ AB \\ \cdots \\ AB \end{bmatrix}.$$

Based on least-square curve fitting, both Eqs. (6) and (7) are transformed as follows:

$$\begin{cases} X_1 = \left(C^{\mathrm{T}}C\right)^{-1}C^{\mathrm{T}}D \\ X_2 = \left(E^{\mathrm{T}}E\right)^{-1}E^{\mathrm{T}}F \end{cases} \tag{8}$$

where A and B present the long and the short axes of ellipse. The elliptical fitting curve of the edges of pore contour that determines the position of equivalent aperture is as follows:

$$\frac{\left(x+\frac{a}{2}\right)^2}{\left(\sqrt{B}\right)} + \frac{\left(x+\frac{b}{2}\right)^2}{\left(\sqrt{A}\right)} = 1 \tag{9}$$

where a and b are the parameters related to the coordinate of center.

Based on the algorithm for ellipse curve fitting above, the holes in CT images are fitted by elliptic curve. Figure 10 presents the effect of the cross section for tibia microstructures. Figure 10a presents the scatter point of the holes in the CT images through ellipse fitting where y represents the elliptical short axis and x represents the elliptical long axis. Based on the method of the maximum simply connected region and proportionate scaling with the real ratio of the area to the pixel value 0.0029 that we obtained, the real cross-section model of structure is represented in Fig. 10b.

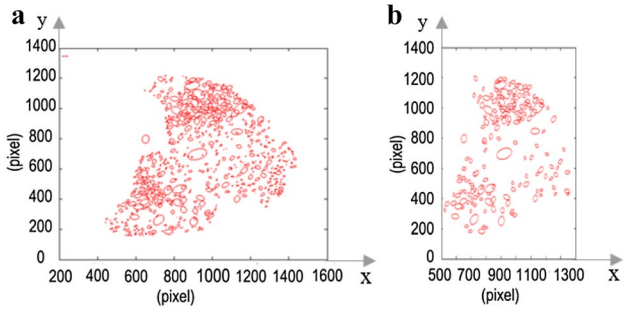

Fig. 10 Illustration of cross section of microstructure for tibia. **a** Before mean value processing; **b** after mean value processing

Experimentations and results

Ellipse fitting

Figure 11 presents the scatter points of the holes in the CT images through ellipse fitting where y represents the elliptical short axis and x represents the elliptical long axis. However, the distribution of points is relatively discrete, and the ratio of the minor axis to the major axis ranges from 0.11 to 0.82. Considering the influence of all points on the structure, we determine the ratio by minimizing the sum of the squares of the errors between these determined ratios and the actual ratios.

The numerical relation between the elliptical length and short axis through least squares straight line fitting is as follows: $y = 0.6501x+4.2645$ where the ratio of the elliptical short axis to long equal is its slope 0.6501. Based on the obtained parameters of area, centroid, ratio of short axis of the ellipse to long and the angle between the major axis and the X-axis of each elliptical object under pixel units, we take the average value of the pixels in each interval as each ellipse area in the corresponding region to fit the scatter points and reconstruct the pore structure characteristics. The elliptic fitting equation based on conical curve is as follows:

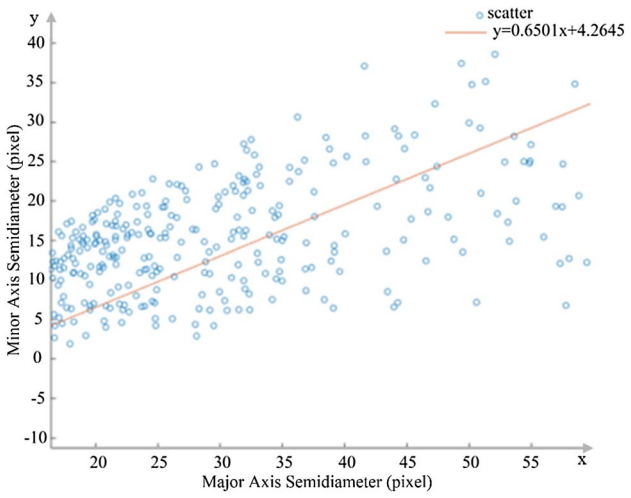

Fig. 11 Illustration of the relationship between short axis and long axis

$$\begin{cases} f(a,(x,y)) = D * a = 0 \\ \Delta(a,x) = \sum_{i=1}^{n} a^{\mathrm{T}} D_i^{\mathrm{T}} D_i a \\ L(a) = \Delta(a,x) - \lambda(a^{\mathrm{T}} C a - \phi) \\ \frac{\partial L(a)}{\partial a} = 0 \\ D = \left(x^2, xy, y^2, x, y, 1\right) \\ a = (a_{xx}, a_{yy}, a_{xy}, a_x, a_y, 1) \end{cases} \tag{10}$$

where $f(a,(x,y))$ represents elliptic function; $L(a)$ represents Lagrange function; λ represents Lagrange multiplier; ϕ represents a positive number; C represents one $6*6$ scatter matrix and $C_{1,3} = C_{3,1} = 2$ and $C_{1,1} = -1$.

Calculation of structural parameters

The patella of patients was upward and both knees were in a straight position. Combined with micro-CT scanning technology and medical orthopedic surgery, corresponding tibia was scanned when patients were in supine position [18]. Cases of tibia tissue were selected to meet the requirement of no disease history of articular surface change caused by arthritis or trauma, no obvious developmental deformity, no obvious degeneration of tibia, and no varus deformity [19]. We scanned tibia from the vertical direction of cross section, with 70 kV voltage, 450 μA current during 500 ms of exposure time. Based on the distance between the longitudinal axis of the tibia and the slide rails of micro-CT set to 30 μm and slice thickness set to 30 μm, we obtained 754 consecutive image sequences. Figure 12 presents 20 image sequences of the representative changing holes.

C represents the circumference of image; ε represents per unit of measurement; and S represents the area. C is proportional to the first power of ε, while S is proportional to the second power of ε on the image. Mandelbrot [12] introduced the method of island replacing the smooth perimeter with fractal circumference. The relation of island above is defined as follows:

$$[C(\varepsilon)]^{\frac{1}{D}} = a_0 \varepsilon^{\frac{1-D}{D}} [S(\varepsilon)]^{\frac{1}{2}} = a_0 \varepsilon^{\frac{1}{D}} \varepsilon^{-1} [S(\varepsilon)]^{\frac{1}{2}} \tag{11}$$

where a_0 is a constant related to the shape of island.

The relation of island extended to 3D graphics is as follows:

$$\left[\frac{C(\varepsilon)}{\varepsilon}\right]^{\frac{1}{D}} = a_0 \varepsilon^{\frac{2-D}{D}} [V(\varepsilon)]^{\frac{1}{3}} \tag{12}$$

Based on the logarithm taking on both sides of the above equality when ε is 1, the obtaining equation is as follows:

$$\log[V] = \log[S]\frac{3}{D} - \log\left(a_0^3\right) \tag{13}$$

The fractal dimension D is as $D = 3/K$ where the slope of log–log plot generated by Eq. (13) is K.

Table 1 gives the sampled data of pore circumference and area in Fig. 12. Figure 13a presents the plot of log–log scatter of the data of perimeter and area by linear fitting in MATLAB. α represents confidence level. Figure 13b presents the residuals in data when α is set to 0.01. Obviously, the width of the short axis is small, the long axis is larger and only one scatter point in 20 scatters is outlier. Furthermore, the scattered point is located near the straight line with the slope equal to 1. There is a good linear correlation between the perimeter and the area parameters in log–log scale coordinates system. So the adjacent pixel points are linear correlation, basically unchanged with the change in gray scale. Pores have significant fractal characteristics. We noted that fractal dimension represents the irregular degree of the edges of pore contour in general, and the fractal dimension of irregular contour curve is between 1 and 3. According to the calculation results, the fractal dimension is 1.741, so the contour is irregular.

Modeling based on support vector machine

The input space is the input vector of the CT image after image processing and its scan slice thickness. By mapping the input space into a high-dimensional feature space with a nonlinear kernel function and the nonlinear transformation system of black box form, we obtained the output vector of the parameters of fractal dimension, porosity and Poisson's ratio. In particular, the equivalent ellipse in the CT images not only includes geometric parameters, but also the number of the equivalent holes and the corresponding interval percentage that is shown in Fig. 9.

Figure 14a presents an identification structure of the black-box model of 3D modeling for CT image. The structure is based on support vector machine corresponding to intermediate nodes. Wang et al. [20] introduced a method of calculating porosity for the holes of the CT images by segmenting and slicing. Hong et al. [21] introduced an experimental measurement method of Poisson's ratio for tibia. Based on support vector machine and a lot of sample tests, we constructed the database of black-box model through imputing the datasets of fractal dimension, equivalent aperture and other parameters. Based on machine learning and the intended target, we find out the function as follows:

$$f(x) = \sum_{i=1}^{n} \left(\alpha_i - \alpha_i^*\right) K\left(x, x_i\right) + b \tag{14}$$

where Mercer kernel function is as follows: $K\left(x_i, x_j\right) = \phi\left(x_i\right) \cdot \phi\left(x_j\right)$; α_i represents Lagrange multiplier; and α_i^* represents the optimal solution of maximum objective function of the formula as follows:

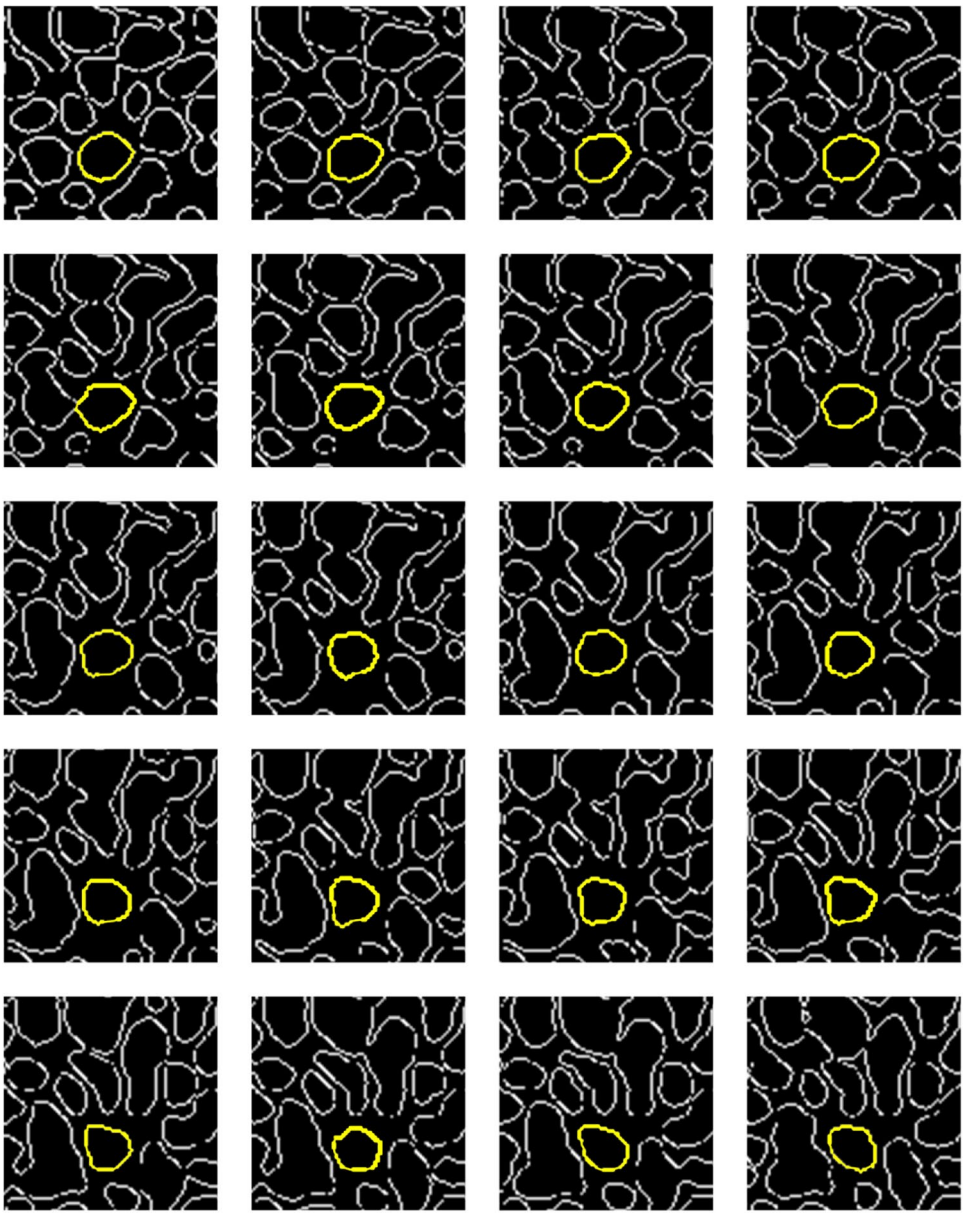

Fig. 12 Gradient microstructure pores of CT image for tibia

$$L(\alpha) = \sum_{i=1}^{N} a_i - \frac{1}{2} \sum_{i=1}^{N} \sum_{j=1}^{N} \alpha_i \alpha_j y_i y_j \left(\phi\left(x_i\right)\right) \cdot \left(\phi\left(x_j\right)\right) \tag{15}$$

$$\begin{cases} f\left(x_i\right) = y_i \\ f : R^d \to R^n, d = 2 \end{cases} \tag{16}$$

$$y(i+1) = f(\phi(i), \theta) \tag{17}$$

where $\phi(i) = \left[y(i), \ldots, y(i-m), u(i), \ldots u(i-n)\right]$; θ presents parameter vector.

Figure 14b presents a mathematic model of the identification structure of 3D modeling.

Discussion

The evaluation criteria of biomimetic scaffold are reconstructed from tissue engineering. In order to satisfy the mechanical, biological and chemical functions and provide a good growth environment for cell attachment, proliferation and differentiation, the criteria need to meet the requirements of bone anatomy such as pore size, porosity, pore shape and pore connectivity. Proper pore parameters ensure the exchange between cells and nutrient solution [15]. Porosity determines the implantation efficiency of cells, molecular diffusion and structural strength of scaffolds. Generally, the structure with high porosity has a high specific surface

Table 1 Software measures the value of perimeter and area of pores on the CT images

Numbers	Perimeter	Area
W1	3.772	0.982
W2	3.772	0.95
W3	3.746	0.979
W4	3.722	0.982
W5	3.85	1.004
W6	3.786	0.993
W7	3.637	0.964
W8	3.619	0.929
W9	3.743	0.971
W10	3.617	0.886
W11	3.568	0.914
W12	3.443	0.855
W13	3.518	0.893
W14	3.652	0.904
W15	3.608	0.906
W16	3.687	0.889
W17	3.524	0.856
W18	3.378	0.786
W19	3.533	0.864
W20	3.568	0.864

area, which is conducive to cell adhesion and distribution [22]. However, scaffolds with higher porosity usually have lower mechanical properties, which is not conducive to the application of tibia implant in surgery [23]. It is reported that when the porosity of the scaffolds is in the range of 50–75%, the mechanical properties and biocompatibility of the scaffolds meet physiological requirements [24]. We reconstruct the tibial microstructure according to pore size and shape, so the corresponding aperture meets anatomical requirements. In order to reconstruct a personalized three-dimensional model of tibia microstructures, we calculate the output vector of fractal dimension, porosity and Poisson's ratio according to formula (14) by inputting CT image. We find the most matching image sequence with ellipse fitting through matching database above. Li [25] introduced an idea of surface rendering of CT image sequence. The methods of judging the connectivity of ellipse are related to the method of corresponding pixels. We reconstruct 3D models by using VC++ environment, surface fitting and linear interpolation between adjacent sequence and judging its connectivity.

Figure 15 presents a bionic model of the microstructure for tibia. In particular, the distance between the sum of radius of the long axis and the short axis of ellipsoid is equal to the distance of its corresponding center points. To obtain the similar three-dimensional structure of natural bone, we keep anisotropy and generate the ellipsoid randomly. The

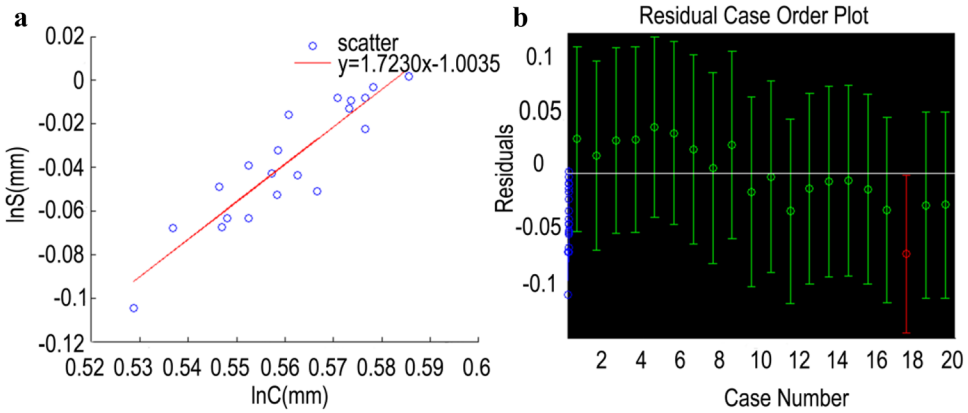

Fig. 13 Log–log graph of perimeters and areas of holes. **a** Illustration of log–log relation; **b** illustration of residuals

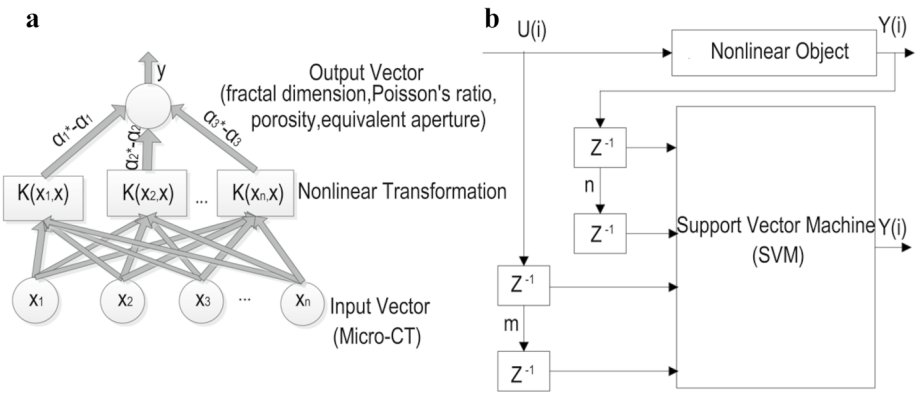

Fig. 14 Illustration of structure identification. **a** Support vector machine; **b** the identification structure

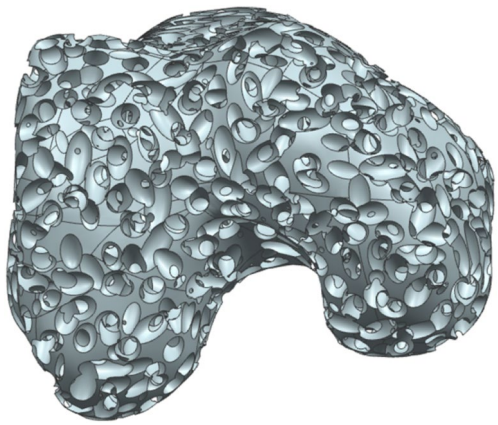

Fig. 15 Illustration of three-dimensional reconstruction for tibia

experimental results show that the three-dimensional structure is well fitted to human tibia, and the porosity is about 70%. The results meet the requirements of porosity and connectivity and provide a good environment for cell adhesion, proliferation, and tissue formation. In addition, the application domain about our proposed method is not limited to tibia. Similar methods can also be used in the construction of bone structure or similar products such as femur and patella.

Conclusions and future work

We have presented a method for digital image preprocessing and edge detection of pore profile for the CT images of tibia. This work carries out two groups of experiments: First, we verify the fractal characteristics of different sequences corresponding to the pore structure; second, we calculate the ratio of the short axis of ellipse fitting to long axis in the pore structure. The above two groups of experiments are designed from the aspect of circumference and area. Based on a large number of CT image sequences, we obtain the relevant parameters. The results of the experiments are given as follows: First, the circumference and area of the corresponding pores have good linear correlation in log–log scale coordinates system, so the pores of the CT images of tibia have fractal characteristics; second, the ratio of the elliptical short axis to the long axis through ellipse fitting tends to be 0.6501, while we obtain a large number of the CT image sequence data.

On the basis, we put forward an individualized CT image modeling method for tibia based on support vector machine. For the three-dimensional reconstruction of bone structure such as femur and patella, or similar products, we provide new methods to reconstruct three-dimensional porous structure during tibia modeling as follows: First, we preprocess the image sequence of pore profiles; second, we detect the contour edges of the images and fit ellipse, followed by calculating the related geometric parameters of ellipse. In the future work, we intend to collect a large number of human bone microstructure imaging samples and build a more complete mapping database among ellipse vector and fractal dimension, porosity, Poisson's ratio and other vectors in order to reconstruct a more satisfying three-dimensional model of bone microstructure for clinical applications.

Acknowledgements This research is supported by the National Key Research and Development Program of China (No. 2016YFC1100600) and the National Nature Science Foundation of China (Nos. 61540006, 61672363).

Compliance with ethical standards

Conflict of interest The authors declare that they have no conflict of interest.

Ethical approval All experiments were verified by simulation and anatomical analysis, and thus, ethical approval is not required.

References

1. Fantini M, Curto M (2017) Interactive design and manufacturing of a Voronoi-based biomimetic bone scaffold for morphological characterization. Int J Interact Des Manuf (IJIDeM) 6:1–12
2. Inal S, Hama A, Ferro M et al (2017) Conducting polymer scaffolds for hosting and monitoring 3D cell culture. Adv Biosyst 1:1700052
3. Chew SA, Danti S (2017) Biomaterial-based implantable devices for cancer therapy. Adv Healthc Mater 6(2):1600766
4. Moghadam MZ, Hassanajili S, Esmaeilzadeh F et al (2017) Formation of porous HPCL/LPCL/HA scaffolds with supercritical CO_2 gas foaming method. J Mech Behav Biomed Mater 69:115
5. Xu S, Lu F, Cheng L et al (2017) Preparation and characterization of small-diameter decellularized scaffolds for vascular tissue engineering in an animal model. Biomed Eng Online 16(1):55
6. Naghieh S, Foroozmehr E, Badrossamay M et al (2017) Combinational processing of 3D printing and electrospinning of hierarchical poly(lactic acid)/gelatin-forsterite scaffolds as a biocomposite: mechanical and biological assessment. Mater Des 133:128–135
7. Chen G, Kawazoe N (2018) Porous scaffolds for regeneration of cartilage, bone and osteochondral tissue. In: Osteochondral tissue engineering
8. Schladitz K (2011) Quantitative micro-CT. J Microsc Oxford 243(2):111–117
9. Silva AMHD, Alves JM, Silva OLD et al (2014) Two and three-dimensional morphometric analysis of trabecular bone using X-ray micro tomography (μCT). Rev Bras Eng Biomédica 30(2):93–101
10. Patel PG, Patel NH (2017) 3D CAD modeling of human knee joint using MIMICS. Int J Appl Innov Eng Manag 6(6):256–264
11. Kamal R, Kumar DA (2013) Three-dimensional (3D) modeling of the knee and designing of custom made knee implant using mimics software. Int J Curr Eng Technol 3(2):327–330
12. Mandelbrot BB (2006) Self-affine fractals and fractal dimension. Phys Scr 32(4):257
13. Yuan J (2010) Eye location under different eye poses, scales, and illuminations. Chin Opt Lett 8(1):59–62

14. Bhargav L, Anu R, Nagaraj D et al (2016) Dynamic resolution of image edge detection technique among Sobel, Log, and Canny algorithms. Int J Sci Res Eng Technol 5(4):206–210
15. Ovsianikov A, Yoo J, Mironov V (2018) 3D printing and biofabrication. Springer, Berlin
16. Fu DL, Jiang QH, He FM et al (2017) Adhesion of bone marrow mesenchymal stem cells on porous titanium surfaces with strontium-doped hydroxyapatite coating. J Zhejiang Univ Sci B 18(9):778–788
17. Chen W, Han S, Qian W et al (2018) Nanotopography regulates motor neuron differentiation of human pluripotent stem cells. Nanoscale 10:3556–3565
18. Ramyar M, Leary C, Raja A et al (2017) Establishing a method to measure bone structure using spectral CT
19. Sun Q, Choudhary S, Mannion C et al (2017) Ex vivo replication of phenotypic functions of osteocytes through biomimetic 3D bone tissue construction. Bone 106:148–155
20. Wang Y, Li X, Que J et al (2015) A porosity calculation method based on CT images and its application. J Hydraul Eng 46(46):357–365
21. Hong J, Cha H, Park Y et al (2007) Elastic moduli and Poisson's ratios of microscopic human femoral trabecular. Springer, Berlin
22. He HY, Zhang JY, Mi X et al (2015) Rapid prototyping for tissue-engineered bone scaffold by 3D printing and biocompatibility study. Int J Clin Exp Med 8(7):11777–11785
23. Han Y, Liu P, Che J et al (2014) Rapid prototyping technology to construct tissue engineering bone scaffold and the in vitro experiment. J Oral Sci Res 30(8):713–716
24. Tseng TLB, Chilukuri A, Park SC et al (2014) Automated quality characterization of 3D printed bone scaffolds. J Comput Des Eng 1(3):194–201
25. Li X (2011) 3D reconstruction of CT/MR images based on improved marching cubes algorithm. Chin J Liq Cryst Disp 26(5):683–687